Supporting Information

Coordination polymer-derived Al^{3+}-doped V_2O_3/C with rich oxygen vacancies for advanced aqueous zinc-ion battery with ultrahigh rate capability

Chang Lin Liu, Yang Liu, Xing Liu and Yun Gong*

Department of Applied Chemistry, College of Chemistry and Chemical Engineering, Chongqing University, Chongqing 401331, P. R. China Tel: +86-023-65678932 E-mail: gongyun7211@cqu.edu.cn

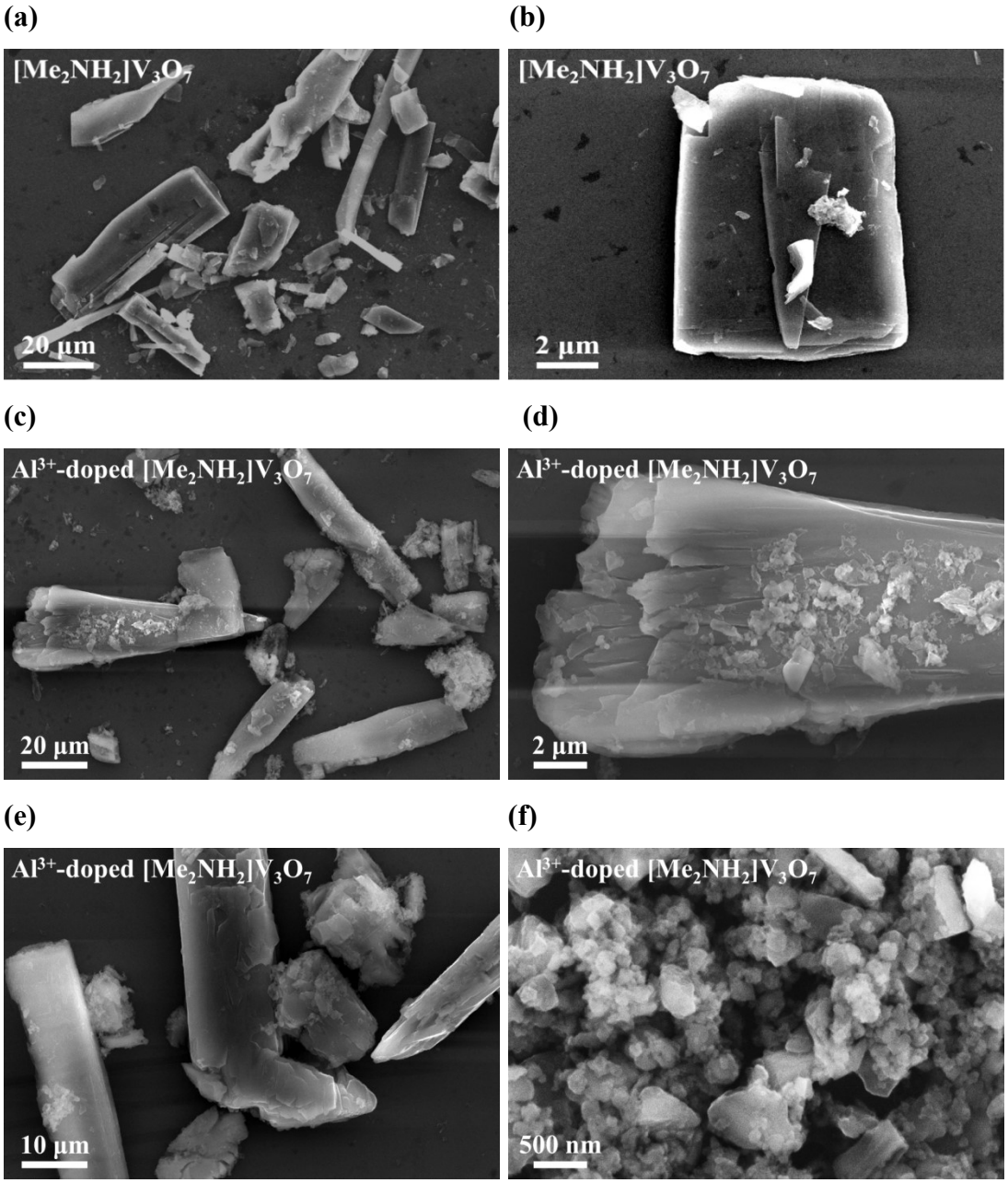

Figure S1 SEM images of (**a, b**) $[Me_2NH_2]V_3O_7$ and (**c-f**) Al^{3+}-doped $[Me_2NH_2]V_3O_7$.

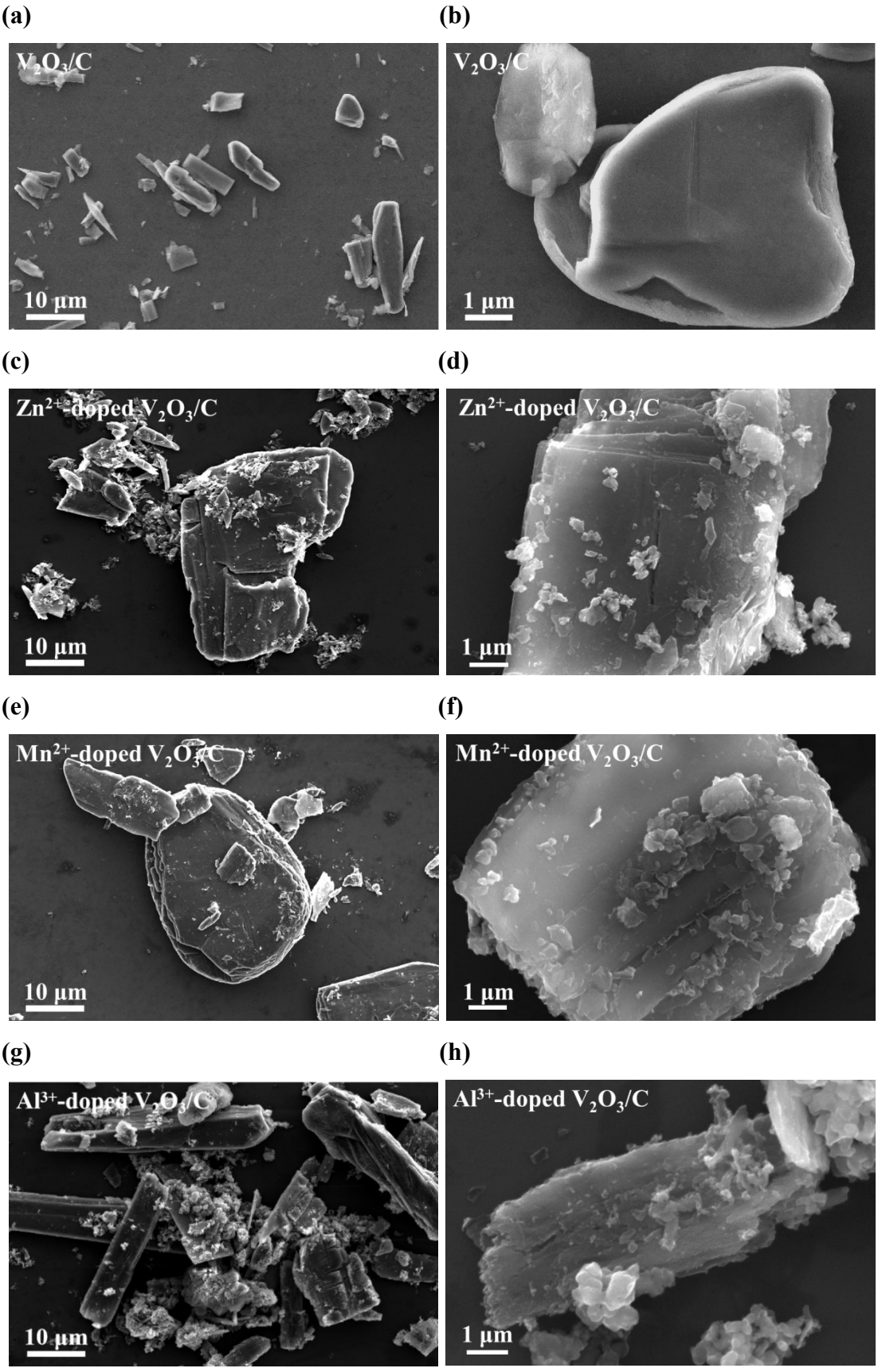

(i)

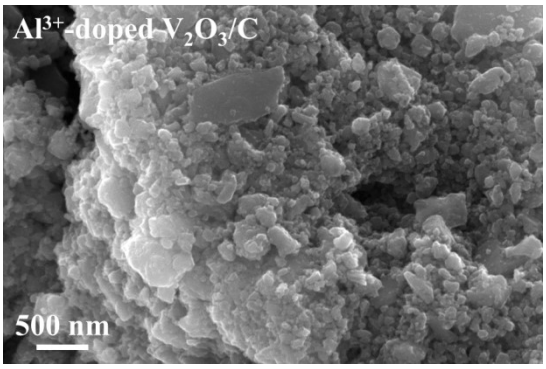

Figure S2 SEM images of (**a, b**) V_2O_3/C, (**c, d**) Zn^{2+}-doped V_2O_3/C, (**e, f**) Mn^{2+}-doped V_2O_3/C and (**g-i**) Al^{3+}-doped V_2O_3/C.

(a)

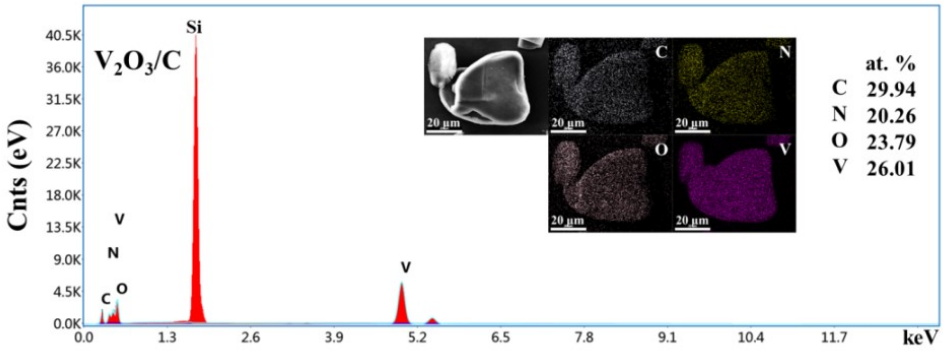

(b)

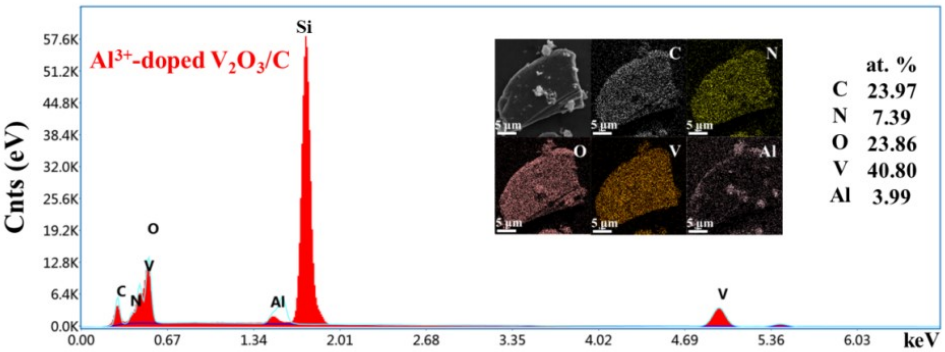

(c)

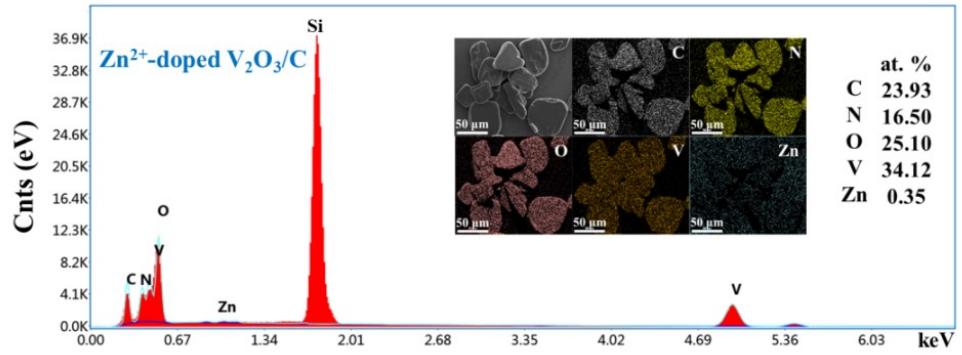

(d)

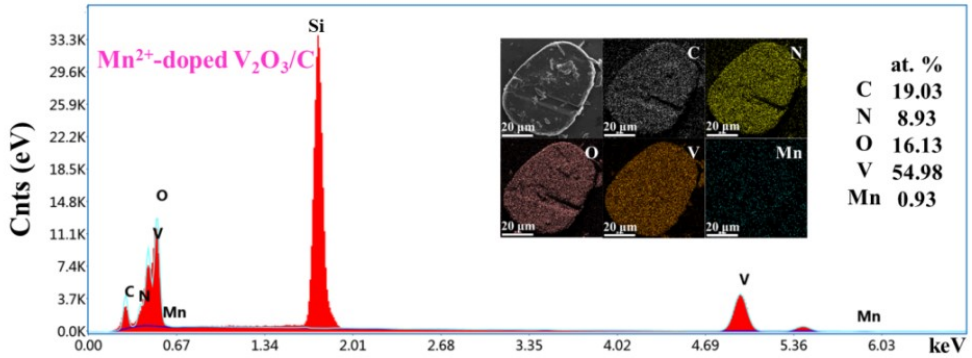

Figure S3 EDS and elemental mappings (inset) of (**a**) V_2O_3/C, (**b**) Al^{3+}-doped V_2O_3/C, (**c**) Zn^{2+}-doped V_2O_3/C and (**d**) Mn^{2+}-doped V_2O_3/C.

S1 Syntheses, compositions and morphologies of $[C_5H_{10}NH_2]V_3O_7$ and V_2O_3/C-p

S1.1 Syntheses of $[C_5H_{10}NH_2]V_3O_7$ and V_2O_3/C-p

The $[C_5H_{10}NH_2]V_3O_7$ precursor was prepared under the same condition except that piperidine ($C_5H_{10}NH$) (0.375 mL, 2.5 mmol) was used instead of DMF (1 mL) in the synthesis of $[Me_2NH_2]V_3O_7$.[1] And V_2O_3/C-p was obtained via the same annealing method except that 100 mg $[C_5H_{10}NH_2]V_3O_7$ precursor was annealed instead of $[Me_2NH_2]V_3O_7$ in the synthesis of V_2O_3/C (**Scheme S1**).

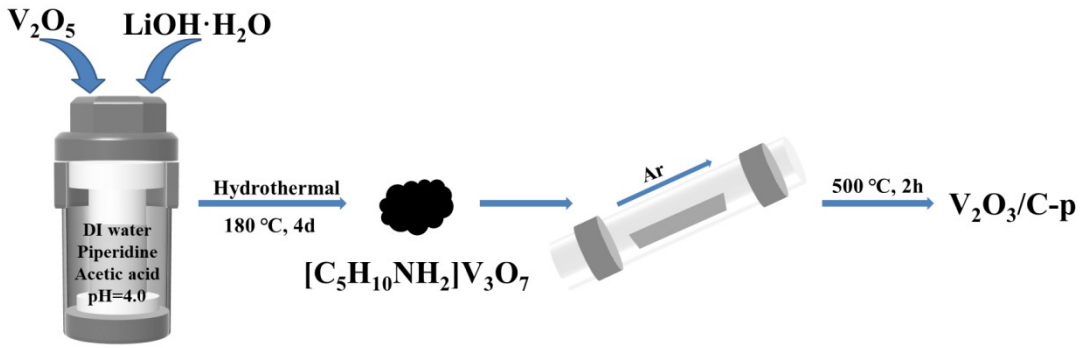

Scheme S1 The synthesis procedures of $[C_5H_{10}NH_2]V_3O_7$ and V_2O_3/C-p.

S1.2 Structure and morphology of $[C_5H_{10}NH_2]V_3O_7$

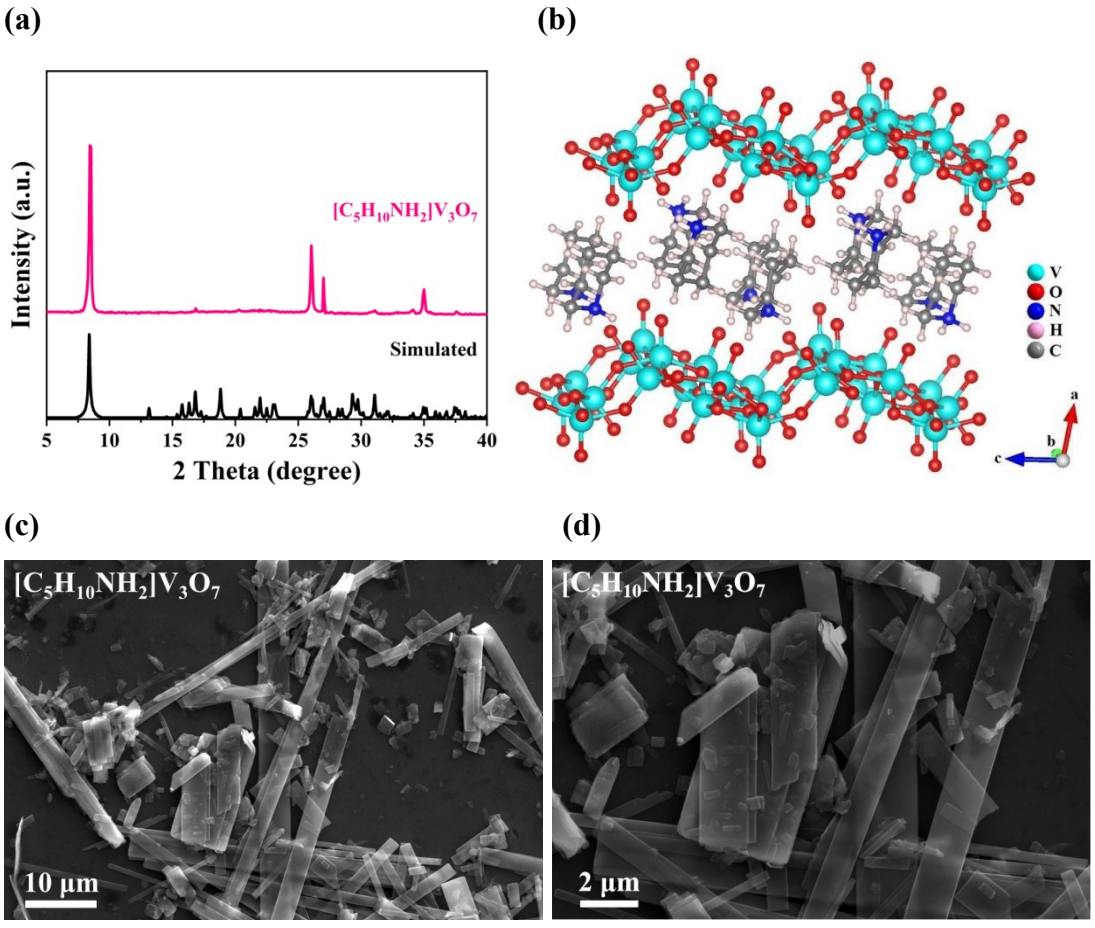

Figure S4 (**a**) XRD pattern of $[C_5H_{10}NH_2]V_3O_7$ and the simulated profile; (**b**) $[V_3O_7]^-$ anionic layers and lamellar $[C_5H_{10}NH_2]^+$ cations in $[C_5H_{10}NH_2]V_3O_7$; (**c, d**) SEM images of $[C_5H_{10}NH_2]V_3O_7$.

The XRD pattern of $[C_5H_{10}NH_2]V_3O_7$ is shown in **Figure S4a**, which meets well with the simulated profile based on the single crystal diffraction data (CCDC No.

235654),[1] indicating the successful preparation of the sample without impurity. As shown in **Figure S4b**, $[C_5H_{10}NH_2]V_3O_7$ possesses the same 2D $[V^{IV}_2V^{V}O_7]^-$ anionic skeleton, however, the interlayer uncoordinated cation is the protonated piperidine cation $[C_5H_{10}NH_2]^+$. The result elucidates the generality for the synthesis of the $[V_3O_7]^-$ -based coordination polymer.

As shown in **Figure S4(c, d)**, the morphology of $[C_5H_{10}NH_2]V_3O_7$ displays regular nanobelts, demonstrating that the different interlayer cations lead to different morphologies.

S1.3 Composition and morphology of V_2O_3/C-p

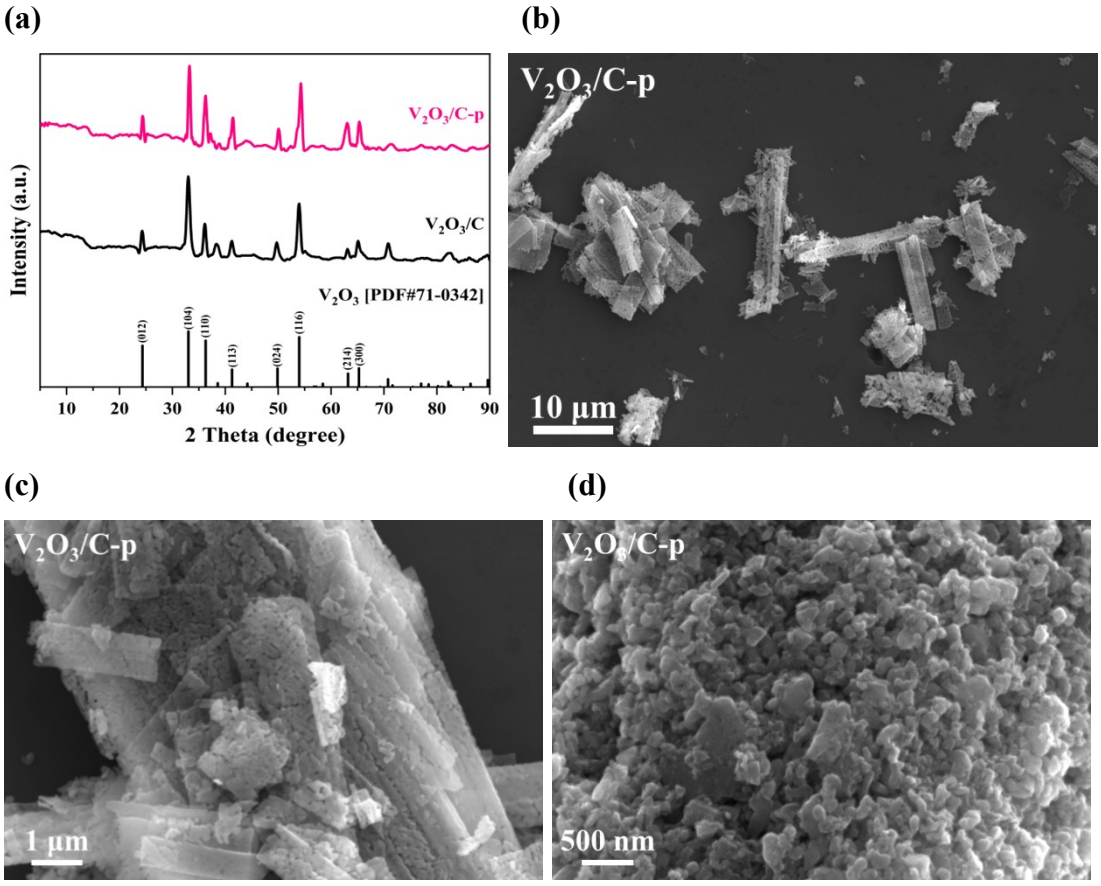

Figure S5 (**a**) XRD pattern and (**b-d**) SEM images of V_2O_3/C-p.

V_2O_3/C-p was synthesized via calcination of $[C_5H_{10}NH_2]V_3O_7$. The XRD pattern of V_2O_3/C-p is shown in **Figure S5a**, which meets well with that of the hexagonal $V^{III}_2O_3$ (PDF#71-0342). Similarly, the broad peak in the range of 10 ~15 ° is attributed to amorphous carbon, which originates from the decomposition of $[C_5H_{10}NH_2]^+$ cations during annealing, inferring the formation of V_2O_3/C composite. The result depicts that regardless of $[Me_2NH_2]V_3O_7$ and $[C_5H_{10}NH_2]V_3O_7$, their

annealed products are both V_2O_3/C composites, which is probably because they possess the same 2D $[V_3O_7]^-$ anionic skeleton.

As shown **Figure S5(b-d)**, similar to the $[C_5H_{10}NH_2]V_3O_7$ precursor, V_2O_3/C-p preserves a nanobelt-like contour, which is composed of numerous nanoparticles (NPs). It is expected that the *in situ*-yielded carbon can combine oxygen to release CO_2 ($C + O_2 \rightarrow CO_2$) during the high temperature annealing process, leading to the formation of the porous nanobelt and the reduction of $[V^{IV}_2V^{V}O_7]^-$ into $V^{III}_2O_3$.

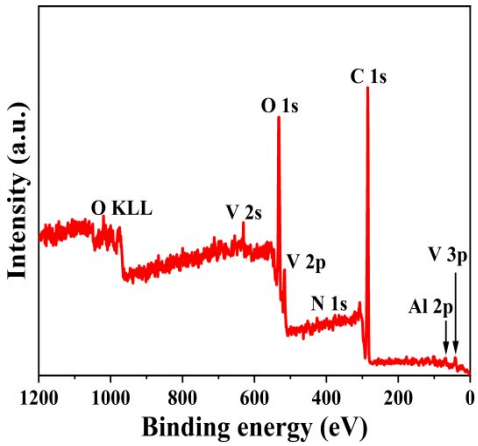

Figure S6 The survey spectrum of Al^{3+}-doped V_2O_3/C.

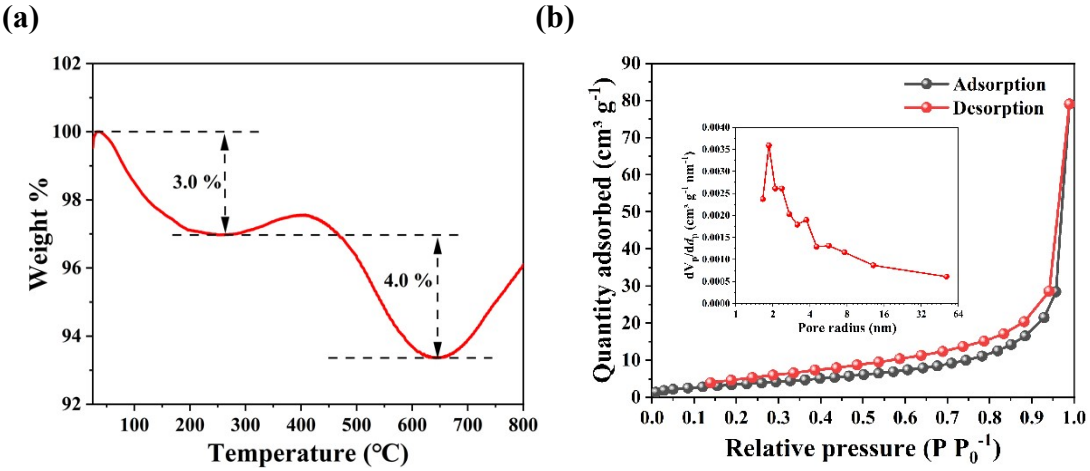

Figure S7 (**a**) TG analysis of Al^{3+}-doped V_2O_3/C; (**b**) Nitrogen adsorption-desorption isotherms and the corresponding pore-size distribution curve (inset) of Al^{3+}-doped V_2O_3/C.

Table S1 The electrochemical performances of Al^{3+}-doped V_2O_3/C in comparison with some vanadium-based materials

Cathode	Electrolyte	Voltage window	Specific capacity	Cycle performance	Ref
$Mg_{0.34}V_2O_5 \cdot 0.84H_2O$	3 M $Zn(CF_3SO_3)_2$	0.1-1.8 V	353 mAh g^{-1} at 0.05 A g^{-1}	97 % retained after 2000 cycles at 5 A g^{-1}	2
VO_2	3 M $Zn(CF_3SO_3)_2$	0.3-1.5 V	357 mAh g^{-1} at 0.1 A g^{-1}	91.2 % retained after 300 cycles at 0.75 A g^{-1}	3
VO_2/rGO	3 M $Zn(CF_3SO_3)_2$	0.3-1.4 V	276 mAh g^{-1} at 0.1 A g^{-1}	99 % retained after 1000 cycles at 4 A g^{-1}	4
$V_2O_5 \cdot nH_2O$	3 M $Zn(CF_3SO_3)_2$	0.2-1.6 V	372 mAh g^{-1} at 0.3 A g^{-1}	71 % retained after 900 cycles at 6 A g^{-1}	5
$V_5O_{12} \cdot 6H_2O$	3 M $Zn(CF_3SO_3)_2$	0.2-1.6 V	354 mAh g^{-1} at 0.5 A g^{-1}	94 % retained after 1000 cycles at 2 A g^{-1}	6
$Na_2V_6O_{16} \cdot 1.63H_2O$	3 M $Zn(CF_3SO_3)_2$	0.2-1.6 V	352 mAh g^{-1} at 0.05 A g^{-1}	90 % retained after 6000 cycles at 5 A g^{-1}	7
$Mg_{0.1}V_2O_5 \cdot H_2O$	3 M $Zn(CF_3SO_3)_2$PAM gel	0.1-1.6 V	470 mAh g^{-1} at 0.1 A g^{-1}	95 % retained after 3000 cycles at 5 A g^{-1}	8
$Zn_2V_2O_7$	1 M $ZnSO_4$	0.2-1.4 V	248 mAh g^{-1} at 0.05 A g^{-1}	85 % retained after 1000 cycles at 4 A g^{-1}	9
$H_2V_3O_8$	3 M $Zn(CF_3SO_3)_2$	0.2-1.6 V	423.8 mAh g^{-1} at 0.1 A g^{-1}	94.3 % retained after 1000 cycles at 5 A g^{-1}	10
$Ba_{1.2}V_6O_{16} \cdot 3H_2O$	2 M $ZnSO_4$	0.3-1.4 V	321.2 mAh g^{-1} at 0.1 A g^{-1}	95.6 % retained after 2000 cycles at 5 A g^{-1}	11
NaV_6O_{15}/V_2O_5	2 M $Zn(CF_3SO_3)_2$	0.2-1.8 V	390 mAh g^{-1} at 0.3 A g^{-1}	92.3 % retained after 3000 cycles at 5 A g^{-1}	12
$Ca_{0.23}V_2O_5 \cdot 0.95H_2O$	3 M $Zn(CF_3SO_3)_2$	0.2-1.6 V	355.2 mAh g^{-1} at 0.2 A g^{-1}	97.7 % retained after 2000 cycles at 5 A g^{-1}	13
$Zn_3V_2O_7(OH)_2 \cdot 2H_2O$	1 M $ZnSO_4$	0.2-1.8 V	213 mAh g^{-1} at 0.05 A g^{-1}	68 % retained after 300 cycles at 0.2 A g^{-1}	14
$V_{10}O_{24} \cdot 12H_2O$	3 M $Zn(CF_3SO_3)_2$	0.7-1.7 V	164.5 mAh g^{-1} at 0.2 A g^{-1}	80.1 % retained after 3000 cycles at 10 A g^{-1}	15
Al^{3+}-doped V_2O_3/C	3 M $Zn(CF_3SO_3)_2$	0.2-1.6 V	375 mAh g^{-1} at 0.2 A g^{-1}	94.7 % retained after 1000 cycles at 5 A g^{-1}	**This work**

S2 Electrochemical performance of V_2O_3/C-p in comparison with that of V_2O_3/C

In order to explore the effect of the morphology on the electrochemical behavior, the rate and cycling performances of V_2O_3/C-p was also measured in comparison with V_2O_3/C. As shown in **Figure S8a**, V_2O_3/C-p can deliver an average capacity of 308,

296, 298, 285, 265 and 195 mAh g^{-1} at 0.1, 0.2, 0.5, 1, 2 and 5 A g^{-1}, respectively, and recover to 335 mAh g^{-1} at 0.1 A g^{-1}, which are higher than those of V_2O_3/C. It is associated with the porous nanobelts built by numerous nanoparticles in V_2O_3/C-p, which is beneficial for the diffusion of electrolyte ions and facilitate the exposure of active sites, thus enhance the storage of Zn^{2+}. However, the cycling performance of V_2O_3/C-p is inferior to that of V_2O_3/C though V_2O_3/C-p can provide a larger initial capacity of 263 mAh g^{-1} at 5 A g^{-1}, it sharply declines to 20 mAh g^{-1} at the end of 1000 cycles with a capacity retention of only 7.6 % (**Figure S8b**), suggesting the porous nanobelts also favor for the capacity decay.

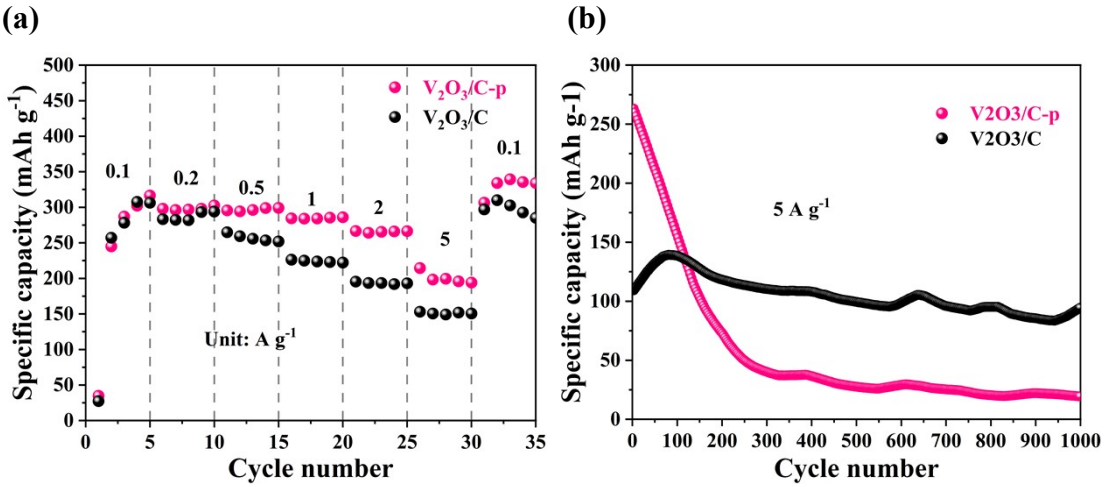

Figure S8 (**a**) Rate capability and (**b**) long-life cycling performances of V_2O_3/C-p in comparison with V_2O_3/C.

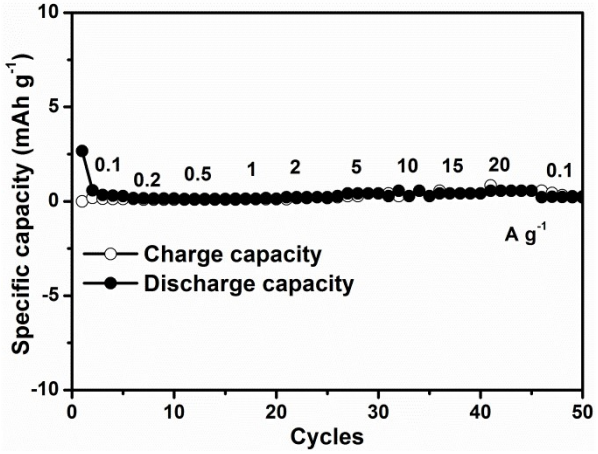

Figure S9 Rate performance of the pure graphite

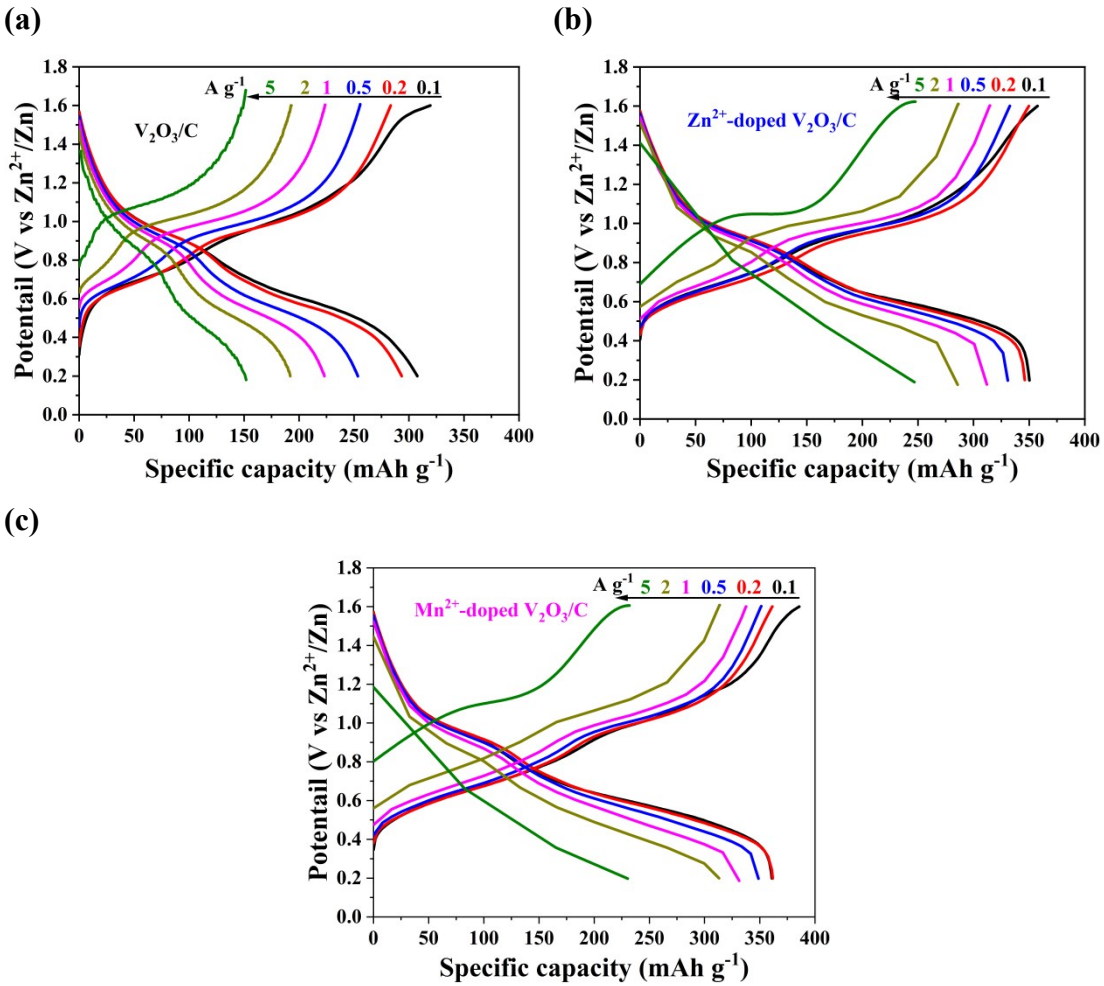

Figure S10 Discharge-charge curves of (**a**) V_2O_3/C, (**b**) Zn^{2+}-doped V_2O_3/C and (**c**) Mn^{2+}-doped V_2O_3/C at various current densities from 0.1 to 5 A g^{-1}.

Table S2 The parameters in the simulated equivalent circuit for Al^{3+}-doped V_2O_3/C and V_2O_3/C

	R_s (Ω cm^{-2})	R_{ct} (Ω cm^{-2})	CPE	R_1 (Ω cm^{-2})
Al^{3+}-doped V_2O_3/C	3.7	5.1	0.7	11.3
V_2O_3/C	2.2	13.5	0.6	8.9

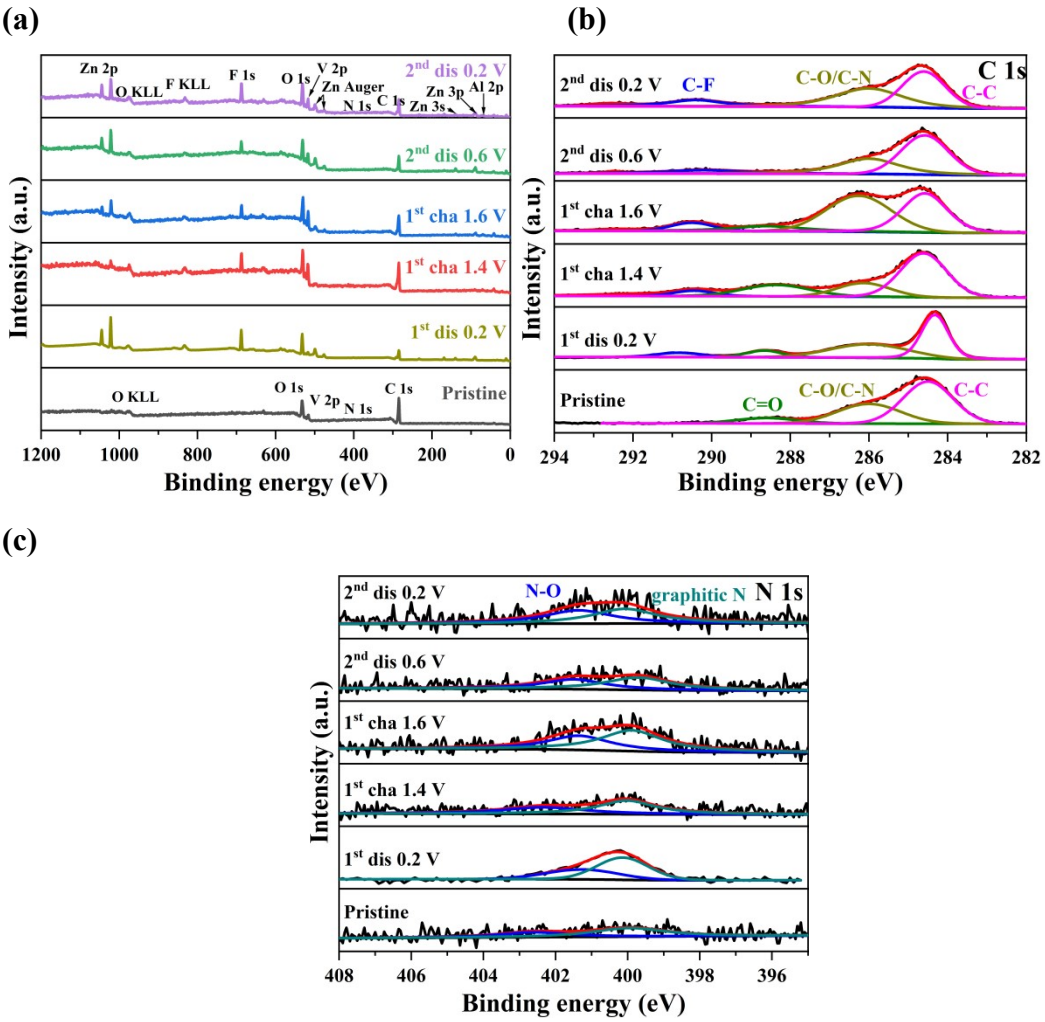

Figure S11 XPS spectra of (**a**) survey, (**b**) C 1s and (**c**) N 1s of the Al^{3+}-doped V_2O_3/C electrode at different states.

S2 *Ex situ* SEM, EDS and elemental mappings of the Al^{3+}-doped V_2O_3/C electrode

In order to obtain deeper insight into the compositional evolution during the discharge/charge process, *ex situ* SEM (**Figure S12a-t**), EDS and elemental mappings (**Figure S13a-j**) of the Al^{3+}-doped V_2O_3/C electrode were performed. As shown in **Figure S12(a, b)**, upon the 1st charge to 0.6 V, the sample exhibits stacked sheets with nanoparticles on the surfaces, which is similar to the morphology of the pristine sample (**Figure S2g-i**). The amount of carbon (64.15 at. %) (**Figure S13a** and **Table S3**) in the discharged cathode is larger than that in the pristine sample (23.97 at. %),

which is mainly due to the addition of conducting agent (graphite and acetylene black) for the fabrication of the electrode. As a result, the Al content is lowered to 1.68 at. % due to the dilution effect of the carbon additive. The F content (6.48 at. %) in the electrode mainly comes from the PVDF binder. Furthermore, the presence of Zn (1.73 at. %) in the discharged electrode illustrates the intercalation of Zn^{2+}. Upon further discharge to 0.2 V, the stacked sheets become loose and the electrode still keeps its original appearance because the 1st discharge process is short (ca. 40 min) (**Figure S12c, d**). Similarly, the morphologies of the Al^{3+}-doped V_2O_3/C electrode are preserved upon the 1st charge to 0.6 (**Figure S12e, f**) and 1.0 V (**Figure S12g, h**). It is consistent with their XRD patterns, which are almost the same as the pristine sample, indicating they maintain the structural integrity of V_2O_3.

However, upon the 1st charge to 1.4 V, XRD pattern discloses the formation of $Zn_3(OH)_2V_2O_7{\cdot}2H_2O$ with the disappearance of V_2O_3, the morphological change of the electrode is minor, which still displays nanoparticles on the surface of sheets (**Figure S12i, j**), indicating the transformation of $V_2O_3 \rightarrow Zn_3(OH)_2V_2O_7{\cdot}2H_2O$ occurs in the inner channel of corrundum-type V_2O_3, which retains the original contour of the pristine sample. Although V_2O_3 is nonporous, the oxygen vacancies in the structure can provide accessible sites for the binding of Zn^{2+}. That is to say, with the oxidation reaction proceeding, the valence state of V is increased, the high-valent V can combine the intercalated Zn^{2+} into $Zn_3(OH)_2V_2O_7{\cdot}2H_2O$. As a result, the amount of oxygen deficiencies is decreased, which is consistent with the O 1s spectra. Similar phenomenon is observed upon deeply charged to 1.6 V. Although the XRD pattern at the fully charged state suggests the further transformation of $V_2O_3 \rightarrow Zn_3(OH)_2V_2O_7{\cdot}2H_2O$, there is not obvious morphological change of the electrode (**Figure S12k, l**). However, as shown in **Scheme 1**, the corrundum-type V_2O_3

possesses a nonporous 3D architecture without free inner space, it is expected the inner accessible sites of V_2O_3 is associated with its rich oxygen vacancies.

Based on XRD data, it is found Al^{3+}-doped V_2O_3/C has been replaced by Al^{3+}-doped $Zn_3(OH)_2V_2O_7{\cdot}2H_2O$/C after the 1st fully charged to 1.6 V, the subsequent discharge/charge process involves the redox reactions of Al^{3+}-doped $Zn_3(OH)_2V_2O_7{\cdot}2H_2O$/C. As a result, upon the 2nd discharge to 1.0 V, ultrathin nanosheets are observed on the outer surface of the Al^{3+}-doped $Zn_3(OH)_2V_2O_7{\cdot}2H_2O$/C sample (**Figure S12m, n**). The ultrathin nanosheets become more and more upon further discharge to 0.6 (**Figure S12o, p**) and 0.2 V (**Figure S12q, r**), which is the result of the H^+ intercalation as evidenced by previous work,[16-18]**.** With the intercalation of H^+ during the 2nd discharge process, the concentration of OH^- in the aqueous solution is excessive, which can combine $Zn_x(CF_3SO_3)_y$ from the electrolyte solution into insoluble $Zn_x(CF_3SO_3)_y$ $(OH)_{2x-y}{\cdot}nH_2O$ on the outer surface of the electrode.[17-19] And the expectation can be proved by the *ex situ* EDS results. As shown in **Figure S13(g-i)** and **Table S3**, the F/S contents in the electrode increase from 5.43/0.15 → 7.55/0.80 → 9.18/1.85 at. % upon the 2nd discharge from 1.0 → 0.6 → 0.2 V. Furthermore, the (de)intercalation of H^+ is almost reversible, upon the 2nd charge to 1.4 V, most of the ultrathin nansheets have disappeared (**Figure S12s, t**) with the F/S contents drop to 6.36/0.24 at. % (**Figure S13j** and **Table S3**).

As for the content of Zn, it is increased from 2.96 → 4.74 → 6.68 at. % from the 2nd discharge to 1.0 → 0.6 → 0.2 V (**Figure S13g-i** and **Table S3**), which originate from the increase of the intercalated Zn^{2+} and adsorbed Zn^{2+} during the discharge process, agreeing with the Zn 2p spectra. And the Zn content drops to 6.68 at. % upon the 2nd charge to 1.4 V (**Figure S13j** and **Table S3**).

(a) **(b)**

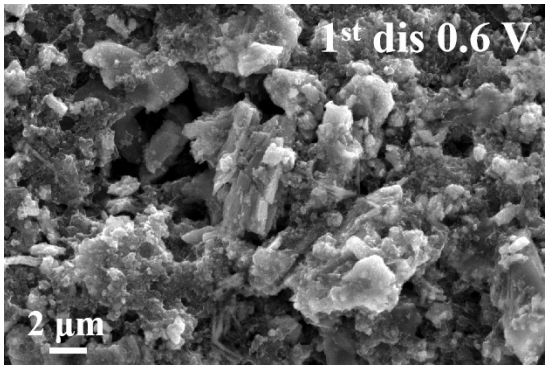
1st dis 0.6 V
2 µm

(c)

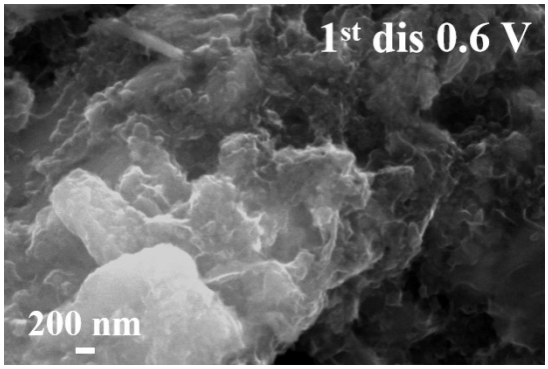
1st dis 0.6 V
200 nm

(d)

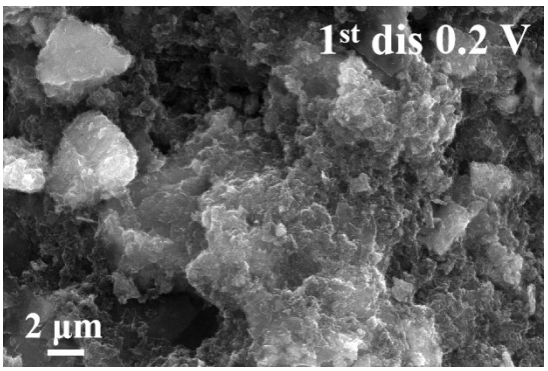
1st dis 0.2 V
2 µm

(e)

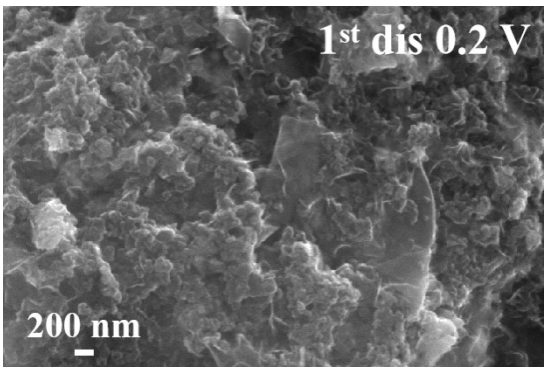
1st dis 0.2 V
200 nm

(f)

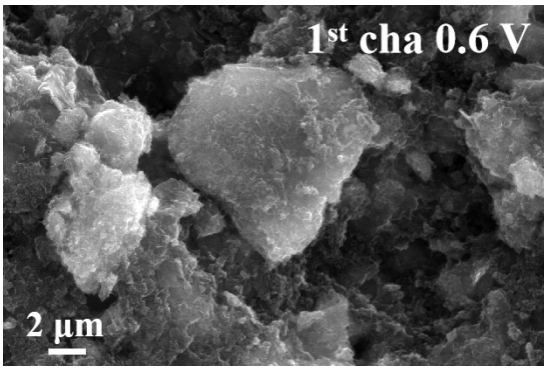
1st cha 0.6 V
2 µm

(g)

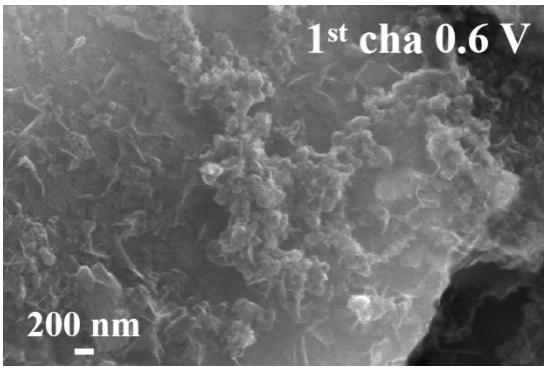
1st cha 0.6 V
200 nm

(h)

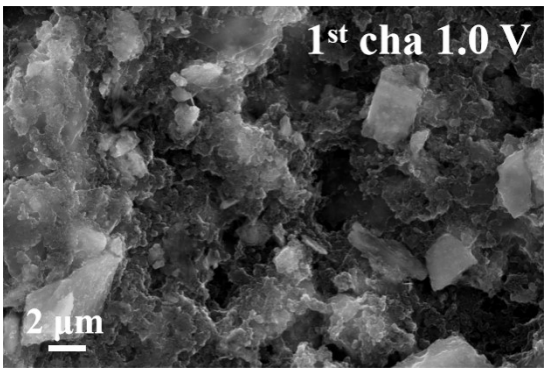
1st cha 1.0 V
2 µm

(i)

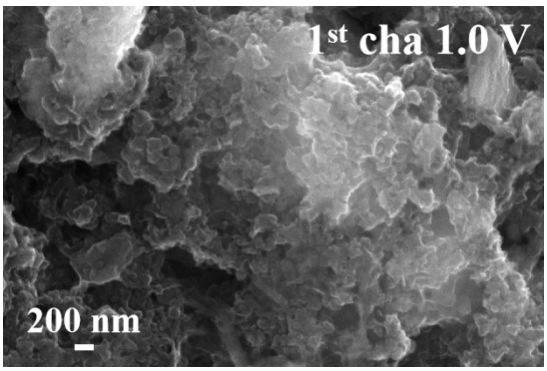
1st cha 1.0 V
200 nm

(j)

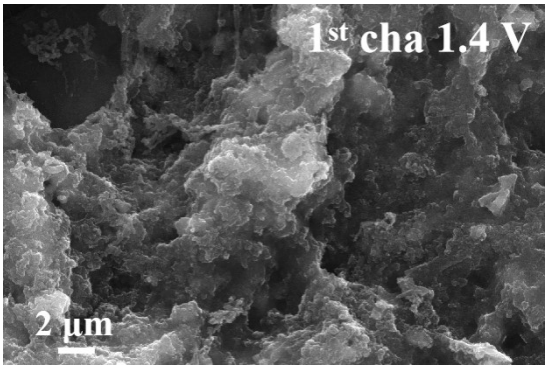
1st cha 1.4 V
2 µm

(k)

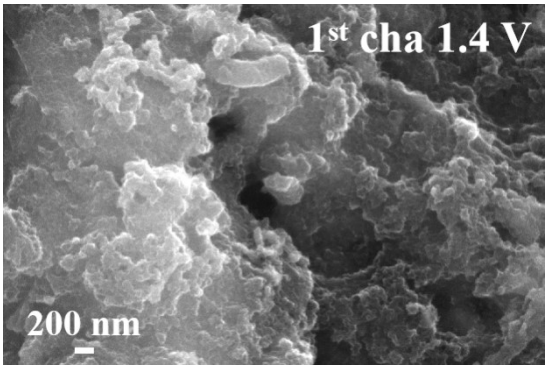
1st cha 1.4 V
200 nm

(l)

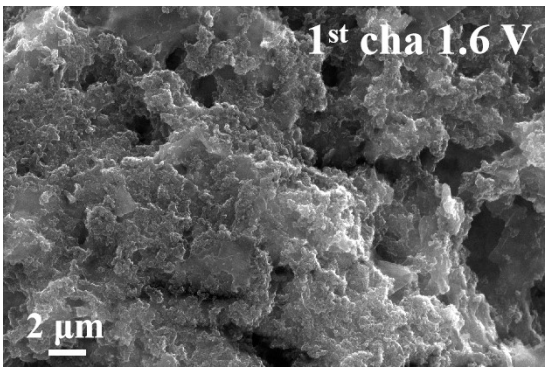
1st cha 1.6 V
2 µm

(m)

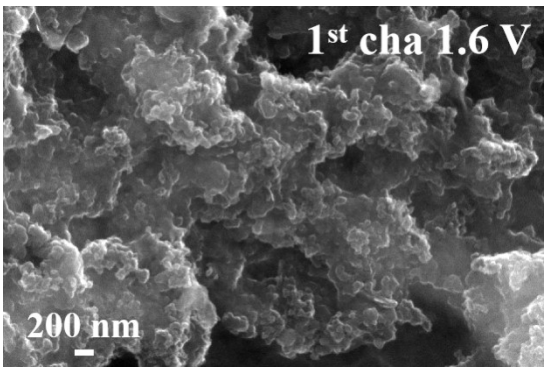
1st cha 1.6 V
200 nm

(n)

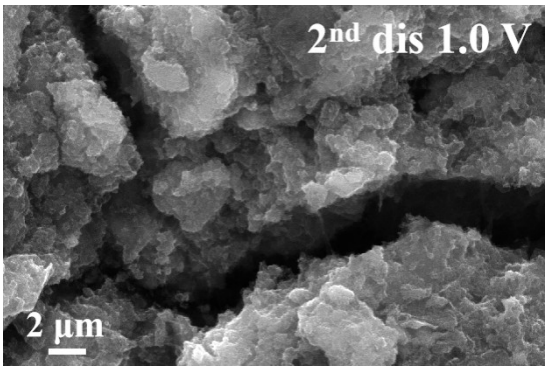
2nd dis 1.0 V
2 µm

(o)

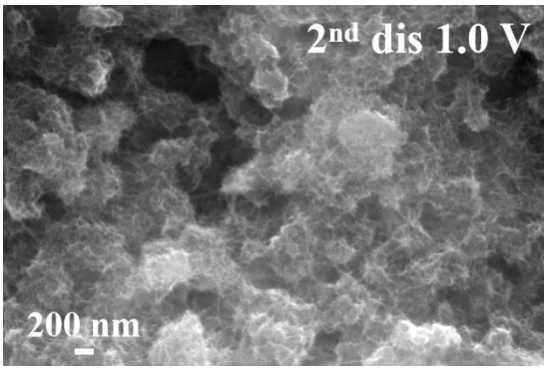
2nd dis 1.0 V
200 nm

(p)

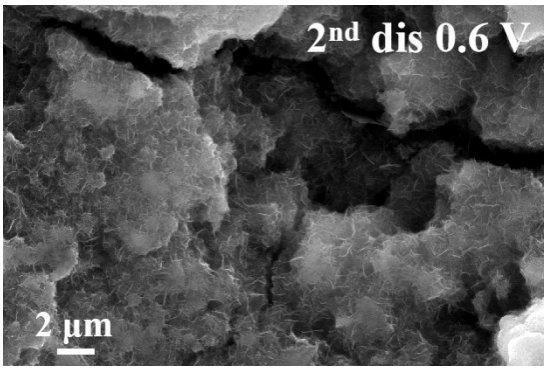
2nd dis 0.6 V
2 µm

(q)

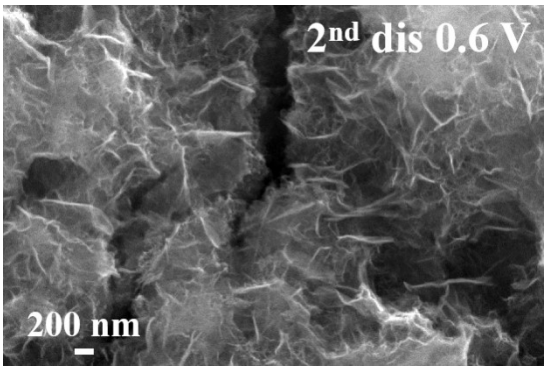
2nd dis 0.6 V
200 nm

(r)

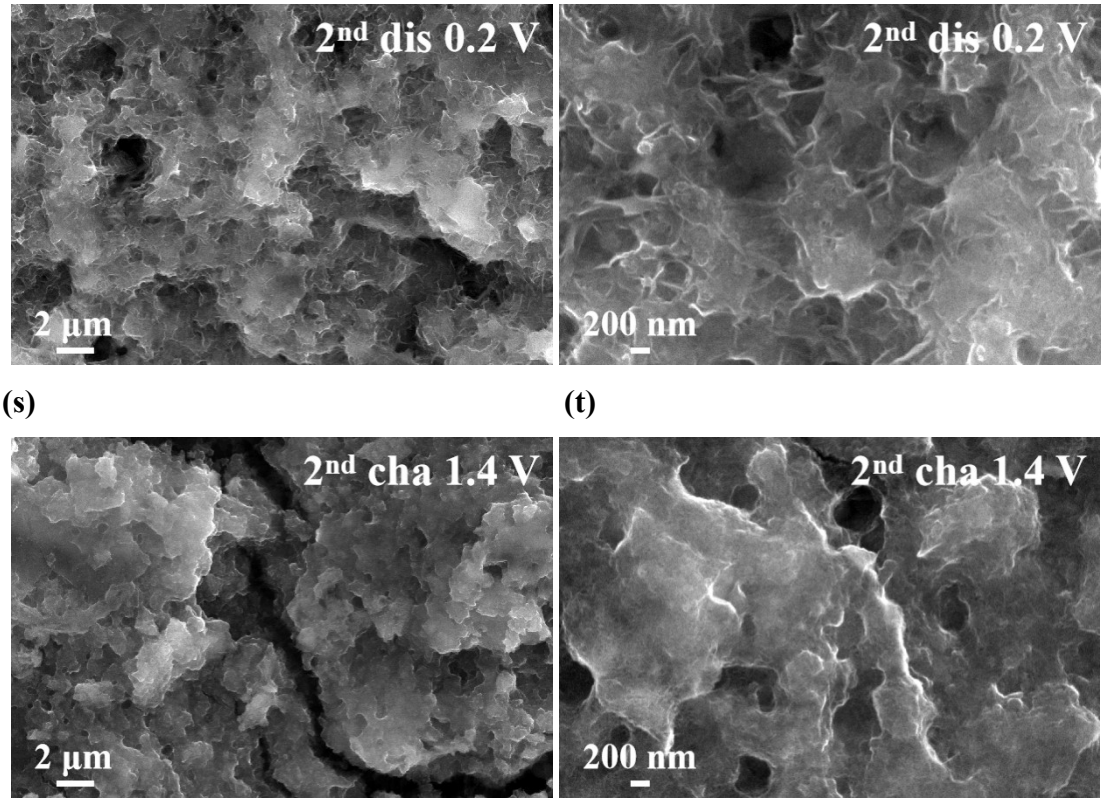

Figure S12 *Ex situ* SEM images of the the Al^{3+}-doped V_2O_3/C electrode at different states: 1st discharge to (**a, b**) 0.6 and (**c, d**) 0.2 V; 1st charge to (**e, f**) 0.6, (**g, h**) 1.0, (**i, j**) 1.4, and (**k, l**) 1.6 V; 2nd discharge to (**m, n**) 1.0, (**o, p**) 0.6 and (**q, r**) 0.2 V; (**s, t**) 2nd charge to 1.4 V.

(a)

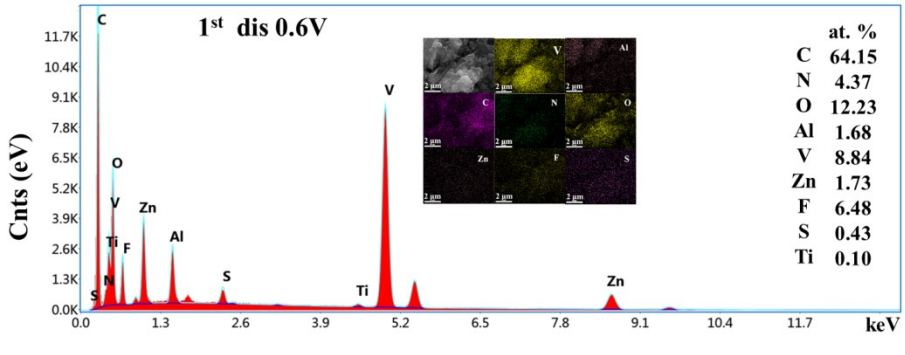

(b)

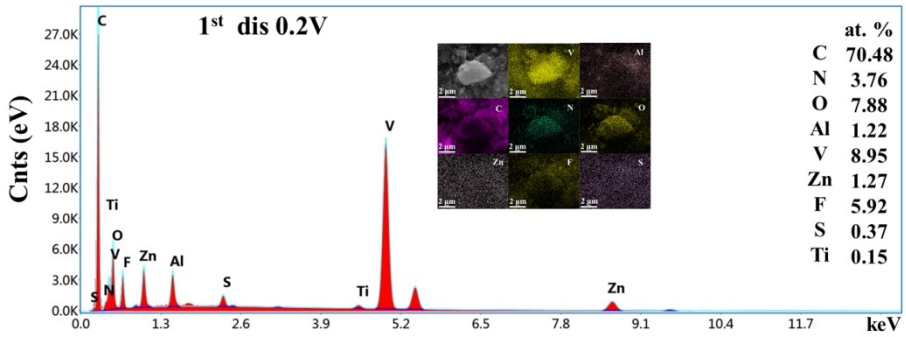
1st dis 0.2V
Cnts (eV)
keV
at. %
C 70.48
N 3.76
O 7.88
Al 1.22
V 8.95
Zn 1.27
F 5.92
S 0.37
Ti 0.15

(c)

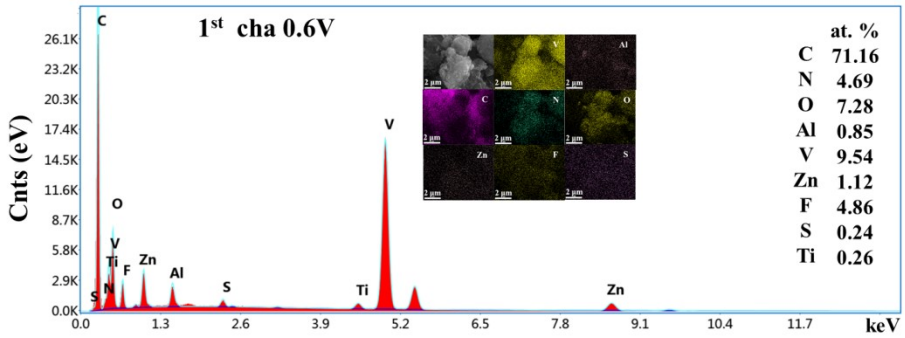
1st cha 0.6V
Cnts (eV)
keV
at. %
C 71.16
N 4.69
O 7.28
Al 0.85
V 9.54
Zn 1.12
F 4.86
S 0.24
Ti 0.26

(d)

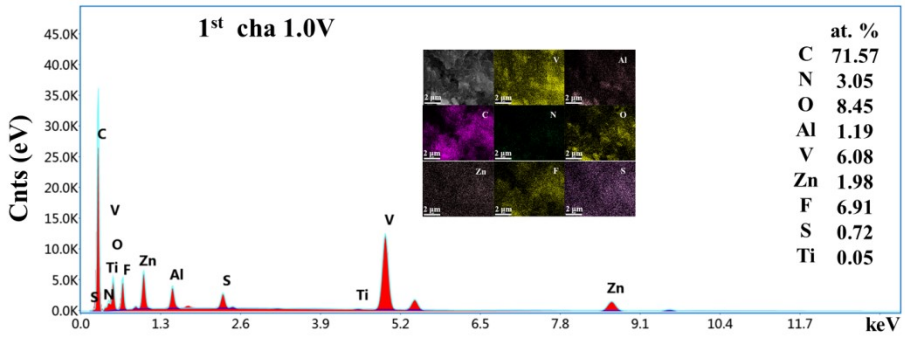
1st cha 1.0V
Cnts (eV)
keV
at. %
C 71.57
N 3.05
O 8.45
Al 1.19
V 6.08
Zn 1.98
F 6.91
S 0.72
Ti 0.05

(e)

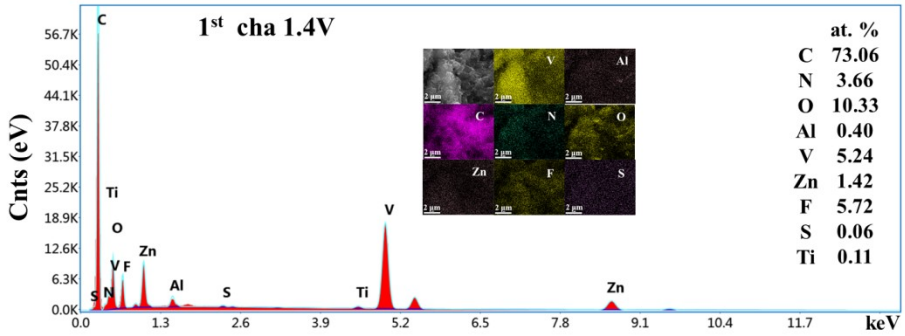
1st cha 1.4V
Cnts (eV)
keV
at. %
C 73.06
N 3.66
O 10.33
Al 0.40
V 5.24
Zn 1.42
F 5.72
S 0.06
Ti 0.11

(f)

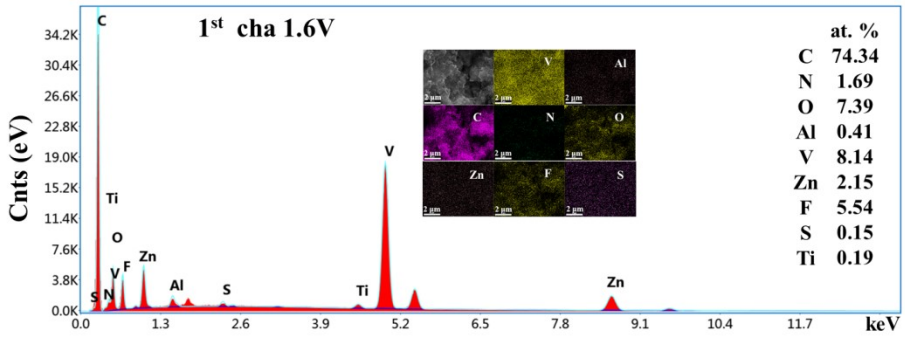
1st cha 1.6V
Cnts (eV)
keV
at. %
C 74.34
N 1.69
O 7.39
Al 0.41
V 8.14
Zn 2.15
F 5.54
S 0.15
Ti 0.19

(g)

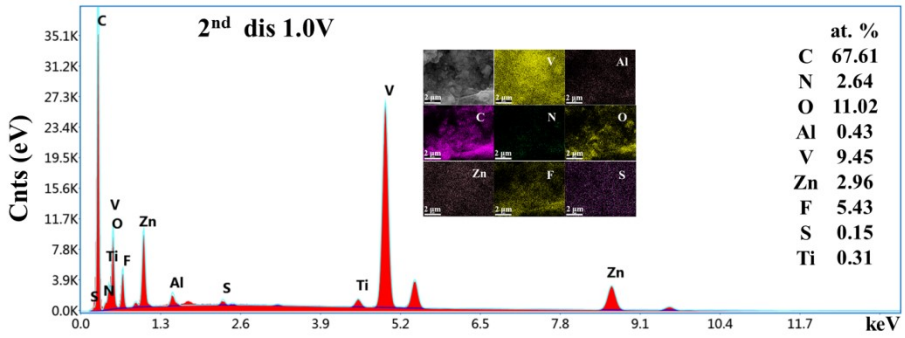
2nd dis 1.0V
Cnts (eV)
keV
at. %
C 67.61
N 2.64
O 11.02
Al 0.43
V 9.45
Zn 2.96
F 5.43
S 0.15
Ti 0.31

(h)

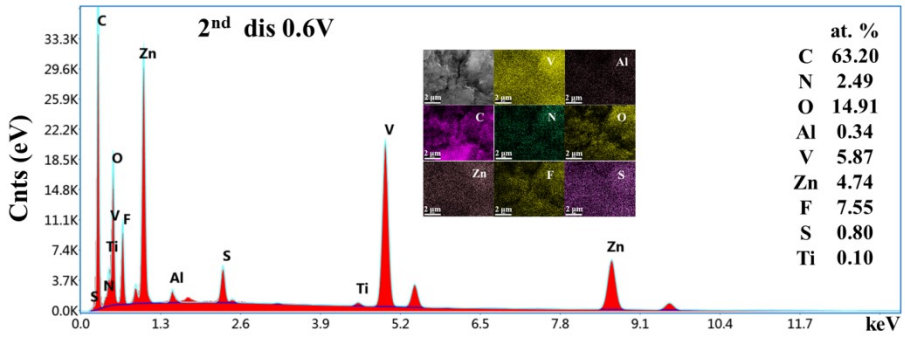
2nd dis 0.6V
Cnts (eV)
keV
at. %
C 63.20
N 2.49
O 14.91
Al 0.34
V 5.87
Zn 4.74
F 7.55
S 0.80
Ti 0.10

(i)

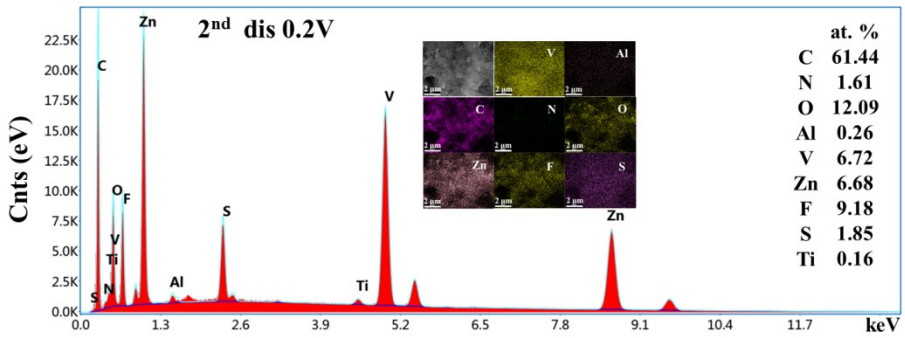
2nd dis 0.2V
Cnts (eV)
keV
at. %
C 61.44
N 1.61
O 12.09
Al 0.26
V 6.72
Zn 6.68
F 9.18
S 1.85
Ti 0.16

(j)

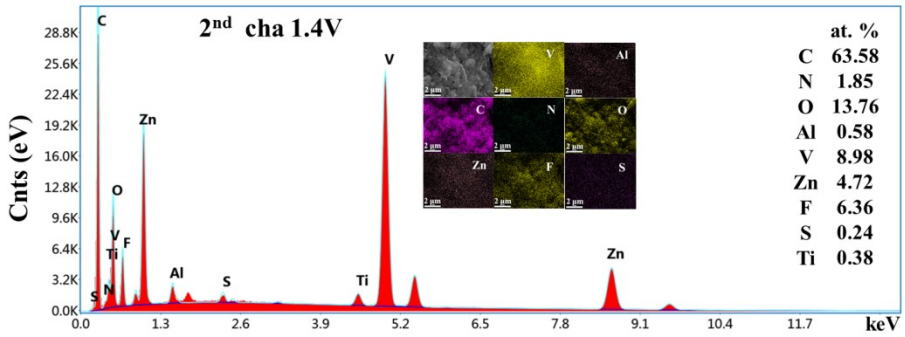

Figure S13 *Ex situ* EDS and elemental mappings of the Al^{3+}-doped V_2O_3/C electrode at different states: 1st discharge to (**a**) 0.6 and (**b**) 0.2 V; 1st charge to (**c**) 0.6, (**d**) 1.0, (**e**) 1.4 and (**f**) 1.6 V; 2nd discharge to (**g**) 1.0, (**h**) 0.6 and (**i**) 0.2 V, (**j**) 2nd charge to 1.4 V.

Table S3 Comparison of the contents of C, N, O, Al, V, Zn, F, S and Ti elements in the Al^{3+}-doped V_2O_3/C electrode at the different states

	C	N	O	Al	V	Zn	F	S	Ti
1st dis 0.6 V	64.15	4.37	12.23	1.68	8.84	1.73	6.48	0.43	0.10
1st dis 0.2 V	70.48	3.76	7.88	1.22	8.95	1.27	5.92	0.37	0.15
1st cha 0.6 V	71.16	4.69	7.28	0.85	9.54	1.1 2	4.86	0.24	0.26
1st cha 1.0 V	71.57	3.05	8.45	1.19	6.08	1.98	6.91	0.72	0.05
1st cha 1.4 V	73.06	3.66	10.33	0.40	5.24	1.42	5.72	0.06	0.11
1st cha 1.6 V	74.34	1.69	7.39	0.41	8.14	2.15	5.54	0.15	0.19
2nd dis 1.0 V	67.61	2.64	11.02	0.43	9.45	2.96	5.43	0.15	0.31
2nd dis 0.6 V	63.20	2.49	14.91	0.34	5.87	4.74	7.55	0.80	0.10
2nd dis 0.2 V	61.44	1.61	12.09	0.26	6.72	6.68	9.18	1.85	0.16
2nd cha 1.4 V	63.58	1.85	13.76	0.58	8.98	4.72	6.36	0.24	0.38

(a)

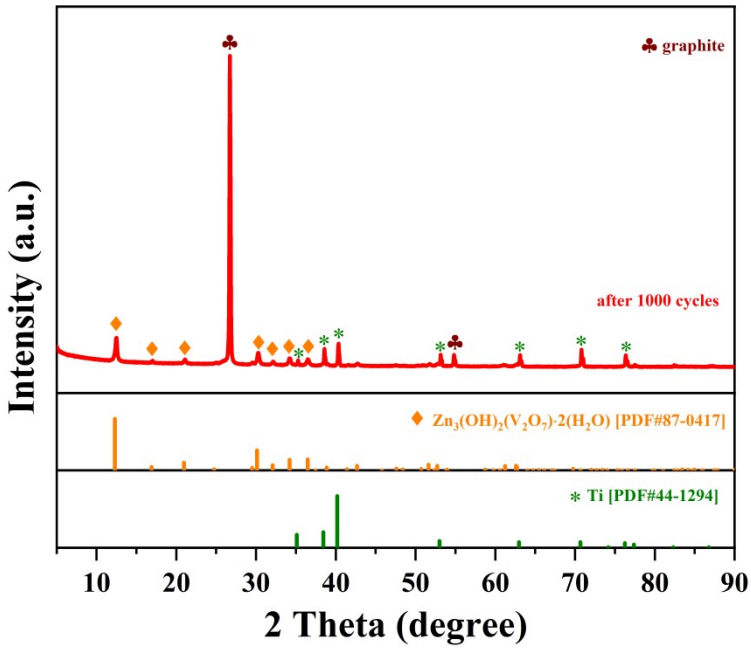

(b)

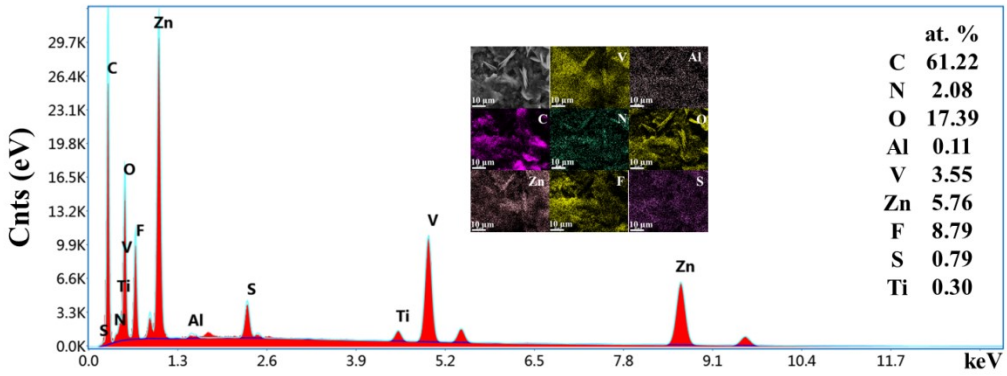

Figure S14 (**a**) XRD pattern and (**b**) EDS as well as elemental mappings (inset) of the Al^{3+}-doped V_2O_3/C electrode after 1000 discharge/charge cycles at 5 A g^{-1}.

(a) (b)

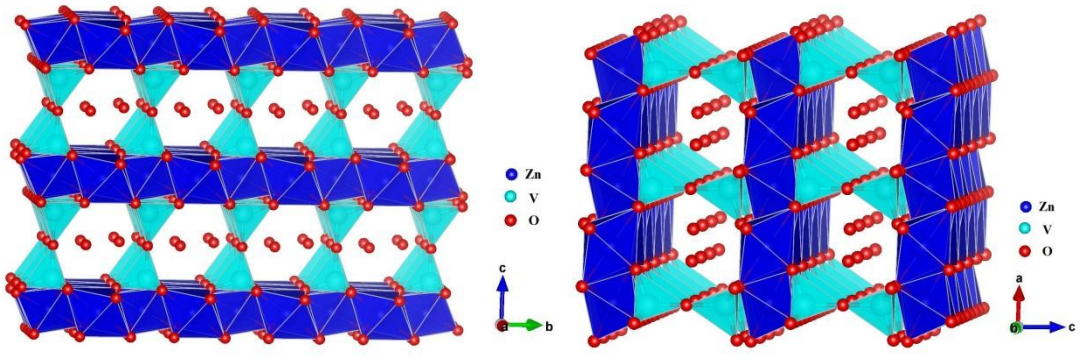

(c) (d)

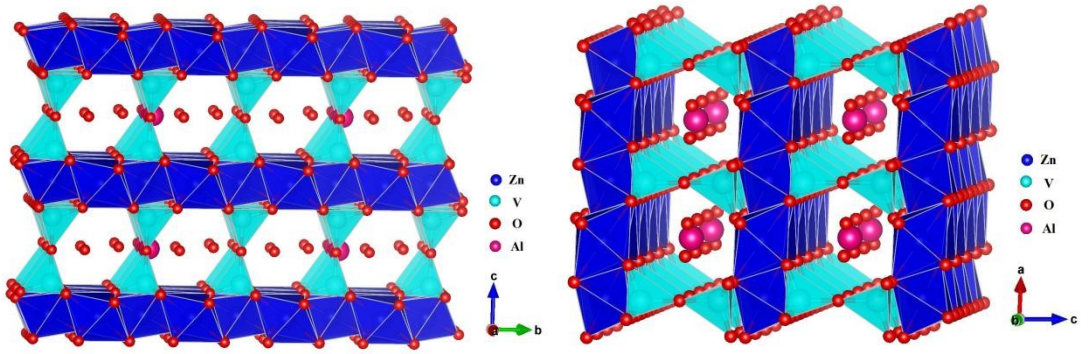

Figure S15 3D architectures of (**a, b**) $Zn_3(OH)_2V_2O_7{\cdot}2H_2O$ and (**c, d**) Al-doped $Zn_3(OH)_2V_2O_7{\cdot}2H_2O$ (H atoms omitted for clarity).

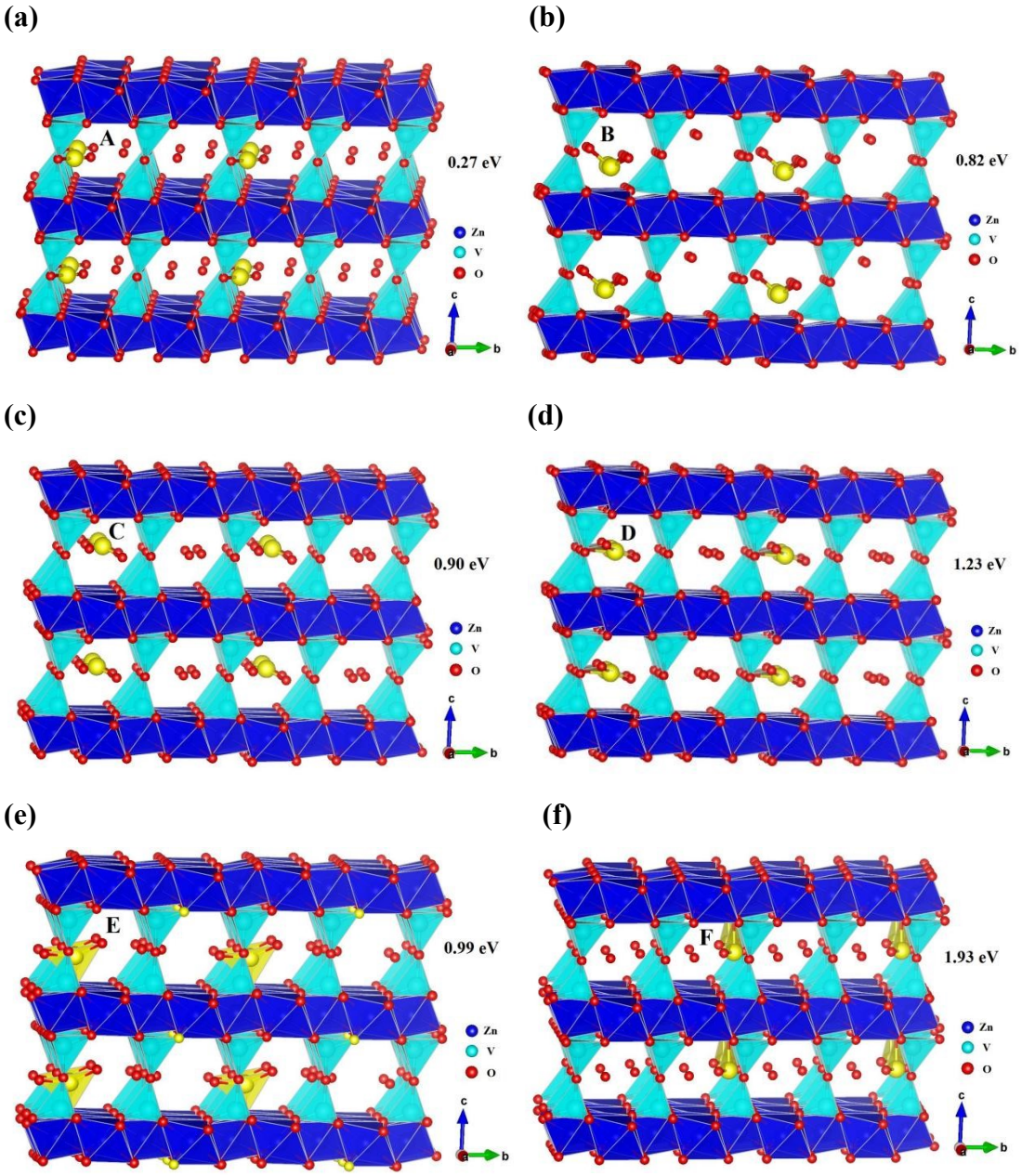

Figure S16 The optimized configurations and the corresponding energies with Zn^{2+} adsorbed on sites (**a**) A, (**b**) B, (**c**) C, (**d**) D, (**e**) E and (**f**) F in $Zn_3(OH)_2V_2O_7{\cdot}2H_2O$ (H atoms omitted for clarity). The intercalated Zn^{2+} ions are denoted in yellow.

Reference

1. S. T. Lutta, N. A. Chernova, P. Y. Zavalij and M. S. Whittingham, *J. Mater. Chem.*, 2004, **14**, 2922-2928.
2. F. Ming, H. Liang, Y. Lei, S. Kandambeth, M. Eddaoudi and H. N. Alshareef, *ACS Energy Lett.*, 2018, **3**, 2602-2609.
3. J. Ding, Z. Du, L. Gu, B. Li, L. Wang, S. Wang, Y. Gong and S. Yang, *Adv. Mater.*, 2018, **30**, e1800762.
4. X. Dai, F. Wan, L. Zhang, H. Cao and Z. Niu, *Energy Stor. Mater.*, 2019, **17**, 143-150.
5. M. Yan, P. He, Y. Chen, S. Wang, Q. Wei, K. Zhao, X. Xu, Q. An, Y. Shuang, Y. Shao, K. T. Mueller, L. Mai, J. Liu and J. Yang, *Adv. Mater.*, 2018, **30**, 1703725.
6. N. Zhang, M. Jia, Y. Dong, Y. Wang, J. Xu, Y. Liu, L. Jiao and F. Cheng, *Adv. Funct. Mater.*, 2019, **29**, 1807331.
7. P. Hu, T. Zhu, X. Wang, X. Wei, M. Yan, J. Li, W. Luo, W. Yang, W. Zhang, L. Zhou, Z. Zhou and L. Mai, *Nano Lett.*, 2018, **18**, 1758-1763.
8. W. Deng, Z. Zhou, Y. Li, M. Zhang, X. Yuan, J. Hu, Z. Li, C. Li and R. Li, *ACS Nano*, 2020, **14**, 15776-15785.
9. B. Sambandam, V. Soundharrajan, S. Kim, M. H. Alfaruqi, J. Jo, S. Kim, V. Mathew, Y. K. Sun and J. Kim, *J. Mater. Chem. A*, 2018, **6**, 3850-3856.
10. P. He, Y. Quan, X. Xu, M. Yan, W. Yang, Q. An, L. He and L. Mai, *Small*, 2017, **13**, 1702551.
11. X. Wang, B. Xi, X. Ma, Z. Feng, Y. Jia, J. Feng, Y. Qian and S. Xiong, *Nano Lett.*, 2020, **20**, 2899-2906.
12. L. Fan, Z. Li, W. Kang and B. Cheng, *J.Energy Chem.*, 2021, **55**, 25-33.
13. W. Zhou, M. Chen, A. Wang, A. Huang, J. Chen, X. Xu and C. P. Wong, *J.Energy Chem.*, 2021, **52**, 377-384.
14. C. Xia, J. Guo, Y. Lei, H. Liang, C. Zhao and H. N. Alshareef, *Adv. Mater.*, 2018, **30**, 7.
15. T. Wei, Q. Li, G. Yang and C. Wang, *Electrochim. Acta*, 2018, **287**, 60-67.
16. L. L. Wang, K. W. Huang, J. T. Chen and J. R. Zheng, *Sci. Adv.*, 2019, **5**, 10.
17. L. Wang, K.-W. Huang, J. Chen and J. Zheng, *Sci. Adv.*, 2019, **5**, eaax4279.
18. M. Du, F. Zhang, X. Zhang, W. Dong, Y. Sang, J. Wang, H. Liu and S. Wang, *Sci China Chem*, 2020, **63**, 1767-1776.
19. W. Leng, L. Cui, Y. Liu and Y. Gong, *Adv. Mater. Interfaces*, 2021, **8**, 2101705.